The Astrophysical Journal, 881:5 (11pp), 2019 August 10 https://doi.org/10.3847/1538-4357/ab2a01

Actinide-rich and Actinide-poor *r*-process-enhanced Metal-poor Stars Do Not Require Separate *r*-process Progenitors

Erika M. Holmbeck[1,2], Anna Frebel[2,3], G. C. McLaughlin[2,4], Matthew R. Mumpower[2,5,6], Trevor M. Sprouse[1], and Rebecca Surman[1,2]

[1] Department of Physics, University of Notre Dame, Notre Dame, IN 46556, USA; eholmbec@nd.edu
[2] JINA Center for the Evolution of the Elements, East Lansing, MI 48824, USA
[3] Department of Physics and Kavli Institute for Astrophysics and Space Research, Massachusetts Institute of Technology, Cambridge, MA 02139, USA
[4] Department of Physics, North Carolina State University, Raleigh, NC 27695, USA
[5] Theoretical Division, Los Alamos National Laboratory, Los Alamos, NM, 87545, USA
[6] Center for Theoretical Astrophysics, Los Alamos National Laboratory, Los Alamos, NM, 87545, USA
Received 2019 March 31; revised 2019 June 10; accepted 2019 June 14; published 2019 August 6

Abstract

The astrophysical production site of the heaviest elements in the universe remains a mystery. Incorporating heavy-element signatures of metal-poor, *r*-process-enhanced stars into theoretical studies of *r*-process production can offer crucial constraints on the origin of heavy elements. In this study, we introduce and apply the "actinide-dilution with matching" model to a variety of stellar groups, ranging from actinide-deficient to actinide-enhanced, to empirically characterize *r*-process ejecta mass as a function of electron fraction. We find that actinide-boost stars do not indicate the need for a unique and separate *r*-process progenitor. Rather, small variations of neutron richness within the same type of *r*-process event can account for all observed levels of actinide enhancements. The very low-Y_e, fission-cycling ejecta of an *r*-process event need only constitute 10%–30% of the total ejecta mass to accommodate most actinide abundances of metal-poor stars. We find that our empirical Y_e distributions of ejecta are similar to those inferred from studies of GW170817 mass ejecta ratios, which is consistent with neutron-star mergers being a source of the heavy elements in metal-poor, *r*-process-enhanced stars.

Key words: binaries: close – nuclear reactions, nucleosynthesis, abundances – stars: abundances – stars: Population II

1. Introduction

The rapid-neutron capture ("*r*-") process is thought to be a main mechanism to synthesize elements heavier than iron, and the only mechanism capable of producing actinide elements, such as thorium and uranium. Astrophysically, possible sites of the *r*-process remain unconfirmed; core-collapse supernovae (CCSNe) and neutron-star mergers (NSMs) are the long-favored candidates. Other, more exotic, *r*-process sites have also been proposed, e.g., dark matter-induced neutron star implosions (Bramante & Linden 2016; Fuller et al. 2017).

CCSNe were thought to be natural sites for robust *r*-process production since Burbidge et al. (1957). Although several studies have shown that current models of CCSNe cannot reproduce the heavy/main elemental *r*-process pattern of the solar system, they may still be responsible for the light *r*-process elements (Thielemann et al. 2011; Arcones & Thielemann 2013). Alternatively, rare types of SNe could contribute to Galactic *r*-process enrichment. The accretion disk around collapsars—the core-collapse of a massive rotating star—has been proposed as a possible site of robust *r*-process element production (Pruet et al. 2004; Surman & McLaughlin 2004). This idea has seen a recent resurgence, and Siegel et al. (2019) argue that the electromagnetic signal from *r*-process production in these events could be veiled by the associated gamma-ray burst. Another possible site is within the jets of magneto-rotational instability-driven SNe (Cameron 2003; Winteler et al. 2012; Nishimura et al. 2015, but see also Mösta et al. 2018).

The recent NSM event GW170817 (Abbott et al. 2017) and corresponding electromagnetic afterglow AT 2017gfo (Cowperthwaite et al. 2017; Drout et al. 2017; Kilpatrick et al. 2017; Shappee et al. 2017) now lends additional observational support for NSMs as robust producers of lanthanide material. Earlier observational evidence in support of NSM was the discovery of the "*r*-process dwarf galaxy" Reticulum II ("Ret II"). In this ultrafaint dwarf galaxy (UFD), high-resolution spectroscopic studies (Ji et al. 2016b; Roederer et al. 2016) identified multiple low-metallicity stars with extreme *r*-process enhancement. Significant *r*-process enrichment in such a small system calls for an event that ejected large amounts of *r*-process material, which Ji et al. (2016a) argue could not be from standard SNe, but could be explained with an NSM.

Simulations suggest that one NSM event houses several environments capable of undergoing an *r*-process. Of particular importance are the neutron-rich, low-entropy dynamical (tidal) ejecta, which escape at high velocities (Lattimer & Schramm 1974; Meyer 1989; Freiburghaus et al. 1999). On a slightly longer timescale is the accretion disk wind, which is estimated to have slightly lower neutron-richness and higher entropy than the tidal ejecta (Metzger et al. 2008; Surman et al. 2008; Perego et al. 2014). Neutrino flavor transformation also has the potential to make the wind significantly more neutron rich than currently predicted by simulation (Malkus et al. 2016).

A well-established method for obtaining empirical evidence on *r*-process sites is through observations of metal-poor stars in the Milky Way halo that are strongly enriched in *r*-process elements. The "*r*-II" stars (defined as $[\mathrm{Eu/Fe}] > +1.0$ and $[\mathrm{Ba/Eu}] < 0$) display a strong relative enhancement of *r*-process elements in their photospheres compared to their iron content (Barklem et al. 2005; Beers & Christlieb 2005). About 3%–5% of stars in the Milky Way halo with $[\mathrm{Fe/H}] \lesssim$

−2 are classified as *r*-II, totaling about 30 *r*-II stars identified as of 2015 (from data in Abohalima & Frebel 2018, "JINAbase"[7]). Outside the Milky Way, about ten UFDs had been studied for *r*-process enrichment as of 2016. At that time, only one—Ret II—was found to have *r*-II stars, with seven (of nine observed) stars identified as *r*-II members (Ji et al. 2016b; Roederer et al. 2016). Given the hierarchical merger origin of the Milky Way (Searle & Zinn 1978; Schlaufman et al. 2009; Tumlinson 2010), metal-poor halo stars likely formed in small early galaxies such as analogs of the surviving UFDs. Accordingly, such strong *r*-process enhancement in halo stars suggests that *r*-process events occurring in these galaxies, such as NSMs that eject large amounts of *r*-process material, should overall be favored as early *r*-process production sites.

Besides the *r*-II stars, there are also the moderately enhanced "*r*-I" metal-poor stars ($+0.3 < [\mathrm{Eu/Fe}] \leqslant +1.0$ and $[\mathrm{Ba/Eu}] < 0$). These stars possibly formed in somewhat larger dwarf galaxies, such as Tucana III (Hansen et al. 2017), in which the yields of any prolific *r*-process event would be diluted more than in the case of the formation of *r*-II stars in smaller systems. The range of both metallicites and level of *r*-process enrichment at which the *r*-I and *r*-II stars are found suggests that NSMs alone could not account for all the *r*-process material in the Galaxy. This idea finds theoretical support in galactic chemical evolution studies; Côté et al. (2019) argue that it is likely that a separate site (or sites) could have contributed *r*-process material at early times in the universe. In addition, cosmological zoom simulations of NSMs may be able to explain *r*-process enrichments of individual dwarf galaxies like Ret II and Tucana III, but cannot simultaneously reproduce Milky Way halo statistics of all *r*-process-enhanced stars (Brauer et al. 2019; Safarzadeh et al. 2019).

The *r*-I and *r*-II stars show striking similarities in their main *r*-process patterns among the lanthanide elements ($_{57}$La through $_{71}$Lu). However, some variation exists in the actinide elements, Th and U, with about 30% showing an enhancement of Th relative to the lanthanides (Mashonkina et al. 2014), dubbed the "actinide-boost" stars. There is also a wider variation of the elemental abundances that follow the first *r*-process peak—Sr, Y, and Zr—with respect to their scaled main *r*-process abundances (Siqueira Mello et al. 2014; Ji et al. 2016a). Due to these variations, it is thought that Sr–Y–Zr may originate from a different *r*-process environment than what produces the lanthanides and actinides, such as the limited-*r*-process, which would primarily synthesize $Z < 56$ elements (Travaglio et al. 2004; Hansen et al. 2012; Arcones & Thielemann 2013; Wanajo 2013; Frebel 2018). Similarly, the actinide variation may indicate a separate *r*-process progenitor object or site that is responsible for the existence of actinide-boost stars (Schatz et al. 2002).

Alternatively, it may be possible that the variations in the actinides and limited-*r* elements in the *r*-I and *r*-II stars can be fully accounted for by variations of astrophysical conditions (e.g., the electron fraction, Y_e) within the same *r*-process source (i.e., type of site). In this work, we identify key elemental abundance measurements of metal-poor, *r*-process-enhanced stars to give insight into the progenitor *r*-process events that gave rise to the observed abundance variations. These key measurements are used in concert with our theoretical "actinide-dilution with matching (ADM)" model to ascertain whether the existence of actinide-boost stars suggests one distinct *r*-process site or if the range of (relative) actinide element abundances can be plausibly explained by a continuum of conditions within the same type of source. With this analysis in hand, we are able to weigh in on the implications of the observations of limited-*r* and actinide elements, and further, to use observations of low-metallicity stars to provide a consistency check on the amount of lanthanide-rich material inferred from recent "kilonova" observations.

In Section 2, we discuss *r*-process patterns of metal-poor stars and quantify distinct differences in their scaled abundances that could reflect different *r*-process sites or conditions among the earliest *r*-process events. In Section 3, we introduce and detail our ADM model. Next, we apply this model to different groups of *r*-process-enhanced stars that were likely enriched by just one event, and we present these results in Section 4. In Section 5, we investigate variations on the astrophysical and nuclear inputs that could affect our model results. Finally in Section 6, we compare our empirical Y_e distributions of mass ejecta to that of the GW170817 associated kilonova to test if our results align with these recent observations.

2. Observations of Metal-poor Stars

In this section, we discuss observations of metal-poor stars in the context of actinide and limited-*r* production. To study the full range of the elemental *r*-process pattern at early times, we choose Zr, Dy, and Th as representative of the limited-*r*-process, main *r*-process, and actinides, respectively. Although $_{38}$Sr and $_{63}$Eu are traditionally used to quantify the limited-*r* and main *r*-process contributions, we instead use $_{40}$Zr and $_{66}$Dy to probe these two regions. More and unsaturated absorption lines of Zr II are available over the few of Sr II from which to derive an abundance, leading to Zr abundances with higher precision. In addition, Sr II suffers larger systematic abundance corrections from assuming local thermodynamic equilibrium (LTE) over non-LTE, while the Zr II corrections are lower and the abundances more robust under LTE (Andrievsky et al. 2011).

In the lanthanide region, the production of Eu by the *r*-process may be sensitive to fission yields, especially to broad and asymmetric fission distributions that place material above the second *r*-process peak (e.g., Kodama & Takahashi 1975; Eichler et al. 2015; Côté et al. 2018; Vassh et al. 2019). Moreover, the fission fragment distributions of nuclei that may participate in the *r*-process at high nuclear masses are far from known. To avoid fission-dependent results, we use Dy instead of Eu. At a slightly higher mass, Dy is less sensitive to (but not entirely free from) the direct effects of fission fragment distributions.

2.1. *Milky Way* r*-process-enhanced Stars*

We first consider all metal-poor Milky Way stars that have both Zr and Dy abundance measurements included in JINAbase and individual additions from the recent discoveries in Placco et al. (2017), Ji & Frebel (2018), Sakari et al. (2018), and Holmbeck et al. (2018). This data set is displayed in the top panel of Figure 1. The absence of stars with both low Zr and high Dy abundances (i.e., upper-left of the top panel of Figure 1) may suggest that some minimum Zr is made in the

[7] https://github.com/abduabohalima/JINAbase

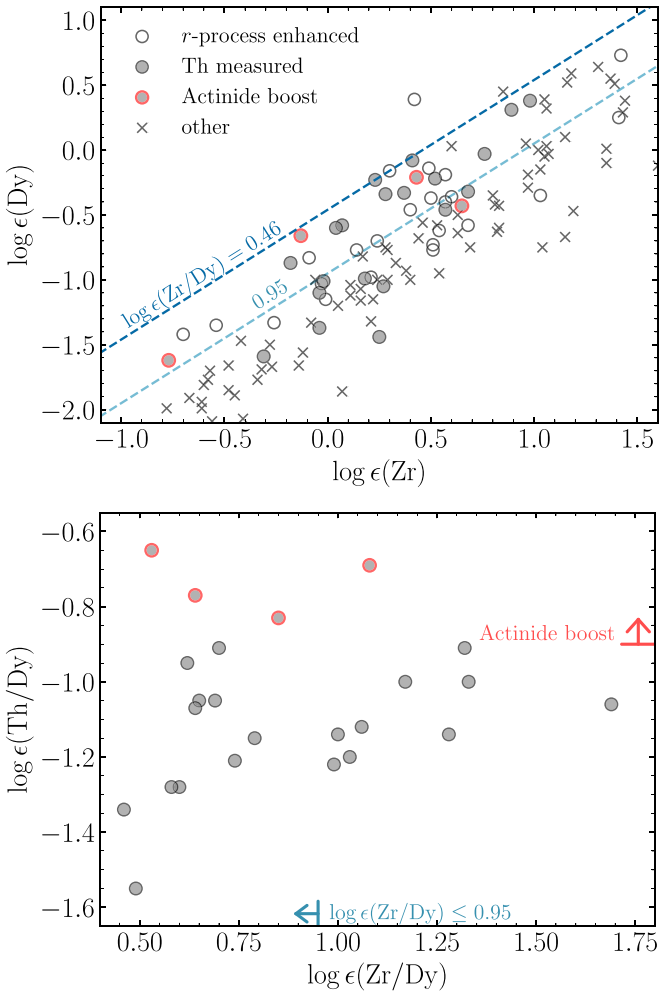

Figure 1. Top: Dy vs. Zr abundances for metal-poor Milky Way stars with an *r*-process signature (circles), a measurement of Th (filled circles), an actinide-boost signature (red outlines), or other enrichment (e.g., *s*-process, *i*-process, and/or carbon enhancement; crosses). The dashed lines are constant values of $\log \epsilon(\mathrm{Zr/Dy})$ of 0.46 and 0.95. Bottom: scatter of $\log \epsilon(\mathrm{Th/Dy})$ as a function of $\log \epsilon(\mathrm{Zr/Dy})$ for those stars with a measurement of Th. Data were selected from Abohalima & Frebel (2018), Placco et al. (2017), Ji & Frebel (2018), Sakari et al. (2018), and Holmbeck et al. (2018).

same event that created Dy. This trend was also noted in Roederer (2013) who analogously used Sr and Ba abundances.

The light and dark blue dashed lines in Figure 1 indicate $\log \epsilon(\mathrm{Zr/Dy}) = 0.95$ and $\log \epsilon(\mathrm{Zr/Dy}) = 0.46$, respectively, for reference and guidance on the abundance trend. Stars with $\log \epsilon(\mathrm{Zr/Dy}) > 0.95$ are mostly those with no *r*-process enhancement (i.e., $[\mathrm{Eu/Fe}] \leqslant +0.3$) and/or with enhancement in other elements, such as carbon and *s*-process elements (e.g., $[\mathrm{Ba/Eu}] \geqslant 0$). The line at $\log \epsilon(\mathrm{Zr/Dy}) = 0.46$ reflects that of the scaled, average $\log \epsilon(\mathrm{Zr/Dy})$ abundance for *r*-process stars in Ret II. We note that all stars with a Th measurement have a $\log \epsilon(\mathrm{Zr/Dy})$ abundance of at least this value. The bottom panel of Figure 1 shows the subset of stars from the top panel that, in addition, have a Th measurement. The wide range of $\log \epsilon(\mathrm{Th/Dy})$ abundances is entirely represented by stars with $\log \epsilon(\mathrm{Zr/Dy}) \leqslant 0.95$. At higher values of $\log \epsilon(\mathrm{Zr/Dy})$, the $\log \epsilon(\mathrm{Th/Dy})$ appears to converge toward a constant value of $\log \epsilon(\mathrm{Th/Dy}) \approx -1.0$.

Most of the confirmed *r*-process-enhanced stars lie in the range $0.46 \leqslant \log \epsilon(\mathrm{Zr/Dy}) \leqslant 0.95$. These stars also show the broadest range of $\log \epsilon(\mathrm{Th/Dy})$. For this work, we posit that these *r*-process stars display a pure *r*-process signature that has come from just one event. For *r*-process stars with $\log \epsilon(\mathrm{Zr/Dy}) > 0.95$, while it is possible that their *r*-process signatures may have also come from a single event, it is also possible that their *r*-process material has been diluted or altered by additional types of nucleosynthesis (i.e., other than a main *r*-process) or strong contributions from limited-*r*-process events. Therefore, to study the widest range of actinide production by a single *r*-process site, we focus on *r*-process stars with $\log \epsilon(\mathrm{Zr/Dy}) \leqslant 0.95$.

2.2. *Kinematically Linked Groups of* r*-process-enhanced Stars*

Given the presumed accretion of stars that now reside in the Milky Way's halo, the *r*-process-enhanced halo stars have essentially unknown origins. Specifically, it has been suggested that the *r*-process-enhanced halo stars originated in dwarf galaxies that were eventually accreted by the Milky Way as part of its hierarchical growth. If a prolific *r*-process event enriched the original, low-mass host galaxy, such as that in Ret II, the imprints on these stars offer a window into the element production by (presumably) single *r*-process events.

Roederer et al. (2018) recently found kinematic grouping among spatially unrelated *r*-process-enhanced halo stars. These kinematic groups are further evidence that *r*-process-enhanced halo stars were once members of satellite galaxies that became accreted by the Milky Way. The progenitor dwarf galaxies of these kinematic groups could resemble Ret II, where all stars belonging to each of these progenitor systems would have formed from gas enriched by single, respective *r*-process events. Therefore, we assume that the elemental abundances of stars in the kinematic groups now reflect the range of element production by single events. Abundance pattern differences among members of each groups could then point to different astrophysical *r*-process conditions within the same type of event or even entirely different *r*-process sources. In this regard, the seven *r*-II stars in Ret II can be treated as an additional such group as it is highly likely that only one *r*-process event took place prior to their formation. Hence, stellar abundance variations within these groups could provide insight into the range of *r*-process element production by a single event.

In the following, we expand on the principal idea of assigning groups of *r*-process stars. Specifically, we focus on elemental abundance variations between these groups in the actinide and limited-*r* elements. Here, we define "actinide-deficient" as $\log \epsilon(\mathrm{Th/Dy}) < -1.20$, "actinide-normal" as $-1.20 \leqslant \log \epsilon(\mathrm{Th/Dy}) \leqslant -0.90$, and "actinide-boost" as $\log \epsilon(\mathrm{Th/Dy}) > -0.90$.

Ret II—Although the scaled, heavy-element (between Ba and the third *r*-process peak) abundance patterns of seven Ret II stars closely resemble those of *r*-II halo stars, the only Ret II member for which a Th measurement is available (DES J033523−540407; Ji & Frebel 2018) displays a strikingly low actinide abundance compared to its lanthanides ($[\mathrm{Th/Eu}] = -0.34$). The seven *r*-II stars of Ret II might reflect an event with low actinide production, or possibly one with a significant range. Without a complete set of Th abundances for each of the *r*-II stars in Ret II, we assume, for simplicity, that this low actinide level reflects low actinide production in the *r*-process event that enriched the Ret II gas. Thus we assume Ret II has $\log \epsilon(\mathrm{Th/Dy}) = -1.49$.

Group F—The kinematic "Group F" in Roederer et al. (2018) consists of three stars: CS 29529-054 (Roederer et al. 2014a, 2014b), HE 2224+0143 (Barklem et al. 2005; Ren et al. 2012), and HD115444 (Westin et al. 2000), the latter two of which have "normal" actinide abundances: [Th/Eu] = 0.05 and [Th/Eu] = −0.21, respectively, and $\log \epsilon(\mathrm{Th/Dy}) = -1.19$ on average.

J0954+5246—Just a single star, but representing extreme levels of actinide production by an *r*-process. 2MASS J09544277 +5246414 ("J0954+5246"; Holmbeck et al. 2018) is currently the most actinide-enhanced *r*-II star known, with [Th/Eu] = 0.38 and $\log \epsilon(\mathrm{Th/Dy}) = -0.65$.

We treat these three levels of relative actinide enhancement as three distinct "groups" and assume that each group's members formed from gas enriched by a individual *r*-process event. Together, the stellar abundances of the stars in Ret II, Group F, and J0954+5246 reflect a range of actinide enhancement, which may indicate either separate *r*-process actinide sources or a variation within one type of *r*-process source.

Between the three groups, the abundances of the limited-*r* elements (Sr, Y, and Zr) also vary with respect to the lanthanide abundances. Whereas it has been suggested that these light neutron-capture elements may originate from a separate *r*-process site, we assume in this analysis that for *r*-process-enhanced stars with $\log \epsilon(\mathrm{Zr/Dy}) \leqslant 0.95$, these elements come from the same event that also synthesized the actinides. Thus, within each group, we consider the relative variations among the limited-*r* elements as well as the actinides as intrinsic to the progenitor *r*-process event.

For this study, we combine the abundances of stars within Ret II and Group F by scaling the individual abundance patterns to the respective average residual obtained from comparison with the solar *r*-process pattern between $_{56}$Ba and $_{71}$Lu. After scaling the solar pattern such that the average deviation of the stellar pattern from solar pattern between Ba to Lu is minimized, we find the range of scaled abundances derived for each element over all stars in Ret II and Group F separately. For J0954+5246, and in the cases where an element was only measured in one star in the group (e.g., Th in Ret II), we use the reported uncertainty in its derived abundance as representative of the "range" for the group. These ranges/uncertainty bands are displayed in Figure 2 for the three enrichment cases. In Section 3, we adopt these scaled and combined abundance values as model input, in order to reconstruct possible distributions of *r*-process material ejected by each of the putative progenitor *r*-process events.

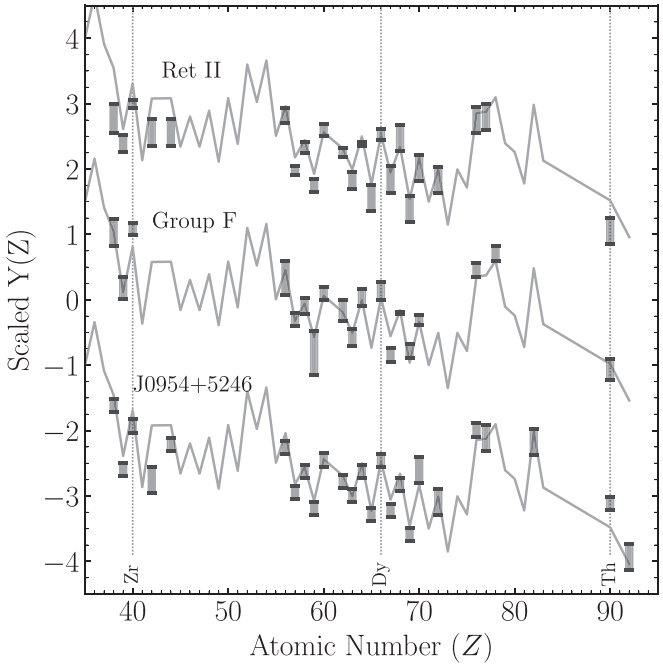

Figure 2. Abundance ranges (arbitrary scaling) of the three stellar groups considered in this work. Solid gray lines show the scaled solar *r*-process pattern.

Table 1
Abundance Ratio Matching Conditions Used by the ADM Method for Each Stellar Group Considered in This Work

Group	#	$\log \epsilon$(Zr/Dy)	$\log \epsilon$(Th/Dy)	$\log \epsilon$(U/Th)
Ret II	7	0.46 ± 0.20	−1.49 ± 0.30	−0.25 ± 0.10
Group F	3	0.95 ± 0.20	−1.19 ± 0.30	−0.25 ± 0.10
J0954+5246	1	0.53 ± 0.20	−0.65 ± 0.30	−0.25 ± 0.10

3. The Actinide-Dilution with Matching Model

The electron fraction (Y_e) is a major factor governing the ultimate extent of element production by an *r*-process event. Variations of how *r*-process ejecta mass is distributed in Y_e may explain the abundance variations within and between stellar groups of *r*-process-enhanced stars, as those described in Section 2. Holmbeck et al. (2019) introduces an actinide-dilution ("AD") model in which a systematic study of Y_e is applied to a mass distribution motivated by literature in order to match scaled actinide-boost stellar abundances. In this section, we build empirical *r*-process ejecta distributions as a function of Y_e by employing a Monte-Carlo method as an extension to the AD model, which we call the ADM model. Rather than start with literature mass distributions, this model constructs mass distributions using stellar abundances as input. To constrain the model by matching results to stellar abundances, we use three particular regions of the observed *r*-process elemental abundance patterns: the limited-*r* group, the lanthanides, and the actinides, represented by Zr, Dy, and Th, respectively. These abundance constraints and their allowed tolerances for the ADM model results are listed in Table 1 for the three groups described in Section 2.2.

Since Th could only be measured in one or two stars per group, the allowed abundance ratios listed in Table 1 come from a single star with the assumption that all other stars within the group have $\log \epsilon(\mathrm{Th/Dy})$ ratios lying with a broad 0.3 dex of that single measurement. Furthermore, we add 0.2 dex to the adopted $\log \epsilon(\mathrm{Th/Dy})$ matching-constraint listed in Table 1. This addition accounts for radioactive Th decay over roughly 10 Gyr from the final abundances of our *r*-process calculations to the present.

Of the three groups in Figure 2, only one star has a reliable uranium measurement, which is unsurprising given that overall, fewer than 10 *r*-process-enhanced stars have a reliable detection of uranium. For stars with both Th and U measurements available, studies applying radioactive decay dating have shown the U/Th production ratio agrees with a roughly constant value, $\log \epsilon(\mathrm{U/Th}) \approx -0.25$, even for the actinide-boost stars which show absolute enhancement in these elements (e.g., Cowan et al. 1999; Schatz et al. 2002; Wanajo et al. 2002; Farouqi et al. 2010).

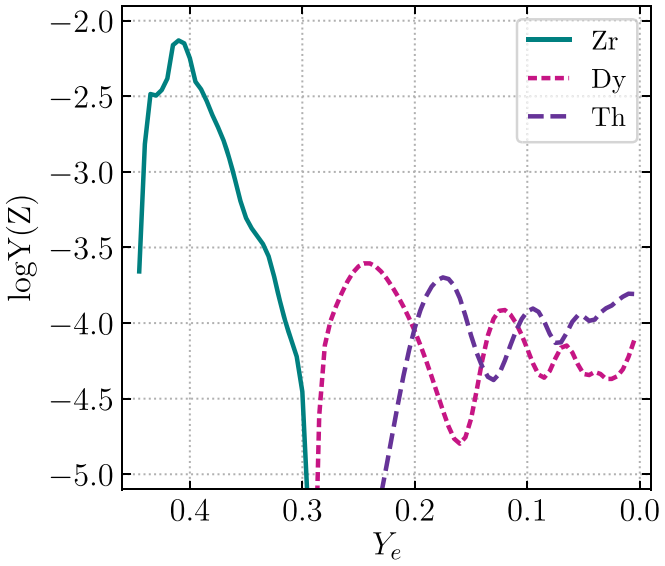

Figure 3. Final Zy, Dy, and Th abundances as a function of Y_e for the disk wind using the FRDM2012 mass model.

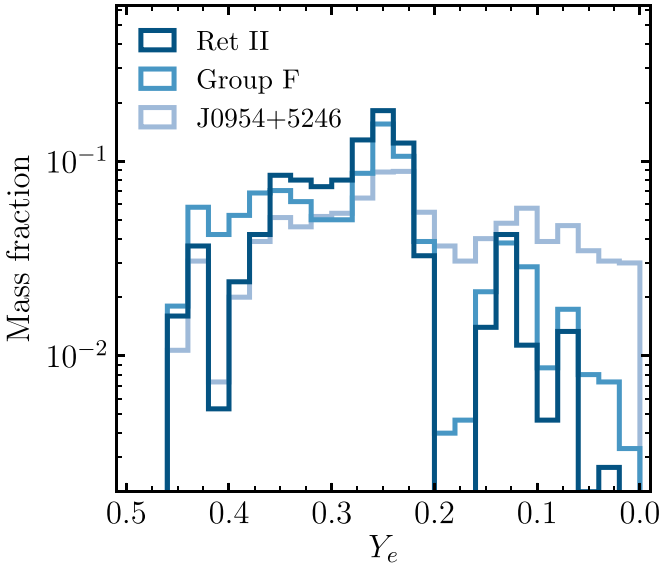

Figure 4. Ejecta distributions characterizing an *r*-process event predicted by the ADM model when matching Ret II, Group F, and J0954+5246 abundances using the disk wind trajectory and the FRDM2012 mass model.

Hence, for this analysis, we assume that the *r*-process material in all stars with Th was produced with the same U/Th ratio, and supply this ratio as an additional constraint to the ADM model. The production ratio rather than the observed ratio is used as Th and U are radioactive, and their abundances change over time.

After establishing the observational constraints, we first ran several *r*-process simulations using a medium-entropy parameterized trajectory (evolution of an ejecta mass element, here with initial entropy $s/k \approx 40$ and dynamical timescale $\tau_{\rm dyn} = 20$ ms) as in Zhu et al. (2018). This trajectory is consistent with an accretion disk wind around a protoneutron star (e.g., a collapsar or NSM remnant; Surman & McLaughlin 2004). We vary the Y_e as in Holmbeck et al. (2019) to allow for multiple levels of neutron-richness within the same environment, changing the initial Y_e from 0.005 to 0.450 in equal steps of 0.005. The *r*-process calculations are run using the nuclear network code, Portable Routines for Integrated nucleoSynthesis Modeling (PRISM, Mumpower et al. 2017, 2018; Côté et al. 2018; Vassh et al. 2019). Reaction and decay rates relevant to the *r*-process are constructed as self-consistently as possible. Starting with nuclear masses from the finite-range droplet model (FRDM2012; Möller et al. 2012, 2016), we adopt the neutron-capture and neutron-induced fission rates calculated self-consistently with FRDM2012 masses using the Los Alamos National Laboratory statistical Hauser-Feshbach code (Kawano et al. 2016). The QRPA+HF framework (Mumpower et al. 2016) is used to calculate the relative probabilities of β-decay, β-delayed fission, and β-delayed neutron emission for each nucleus, using Möller et al. (2019) β-decay strength functions. Fission barrier heights from Möller et al. (2015) are used to calculate fission rates, employing the Zagrebaev et al. (2011) relation for the spontaneous fission channel and adopting symmetric fission fragment distributions for all fission channels.

Figure 3 shows the final calculated Zr, Dy, and Th abundances as functions of Y_e. At the highest values of Y_e considered, a large amount of limited-*r* material around the first *r*-process peak (here, Zr) is synthesized, yet material does not move much beyond the second *r*-process peak ($A \approx 130$, $Z \approx 54$) until $Y_e < 0.30$. With decreasing Y_e, the lanthanides (Dy) are produced, and actinide (Th) production begins at $Y_e < 0.23$. The oscillatory behavior of the lanthanide and actinide abundances at very low Y_e are due to fission cycles that occur in very neutron-rich environments (as discussed in detail in Holmbeck et al. 2019).

With final abundances generated as functions of Y_e, we randomly select N number of Y_e's between 0.005 and 0.450 and the corresponding final Zr, Dy, Th, and U abundances. We choose $N = 15$ to minimize computational time, allow the results to converge, and robustly probe the entire Y_e range. Results generally converge with $N \geqslant 8$. Next, we add the total Zr, Dy, Th, and U abundances over the N randomly selected values. If the total log ϵ(Zr/Dy), log ϵ(Th/Dy), and log ϵ(U/Th) abundances are within the specified constraints of Table 1, we keep all N Y_e's. We repeat this sampling until we accumulate 100 successes, summing a total of 100N individual abundance patterns. When combined, the summed abundances pattern matches the relative observational Zr, Dy, Th, and U abundances for a given kinematic group within the listed tolerances.

4. ADM Model Results

Figure 4 shows the empirical *r*-process ejecta distribution results of the ADM model applied to the three stellar cases discussed in Section 2.2. The empirical mass ejecta distributions that characterize the observed abundance ratios of Ret II, Group F, and J0954+5246 mainly differ in the very low-Y_e tail ($Y_e < 0.18$ in this trajectory) where robust fission cycling and actinide production occurs. The low actinide abundance constraints of the Ret II group allows less mass in this very low-Y_e tail to be ejected, while the actinide-normal Group F and actinide-boost J0954+5246 allow increasing amounts of this fission-cycled material.

The bulk of the mass of material (at $Y_e \geqslant 0.18$) maintains a similar shape in all three cases, including a strong preference for $Y_e \approx 0.25$ and a dip in ejecta production at $Y_e \approx 0.18$. The peak occurs because the log ϵ(Th/Dy) ratio is satisfied near $Y_e \approx 0.25$ for all three cases. On the other hand, the dip at

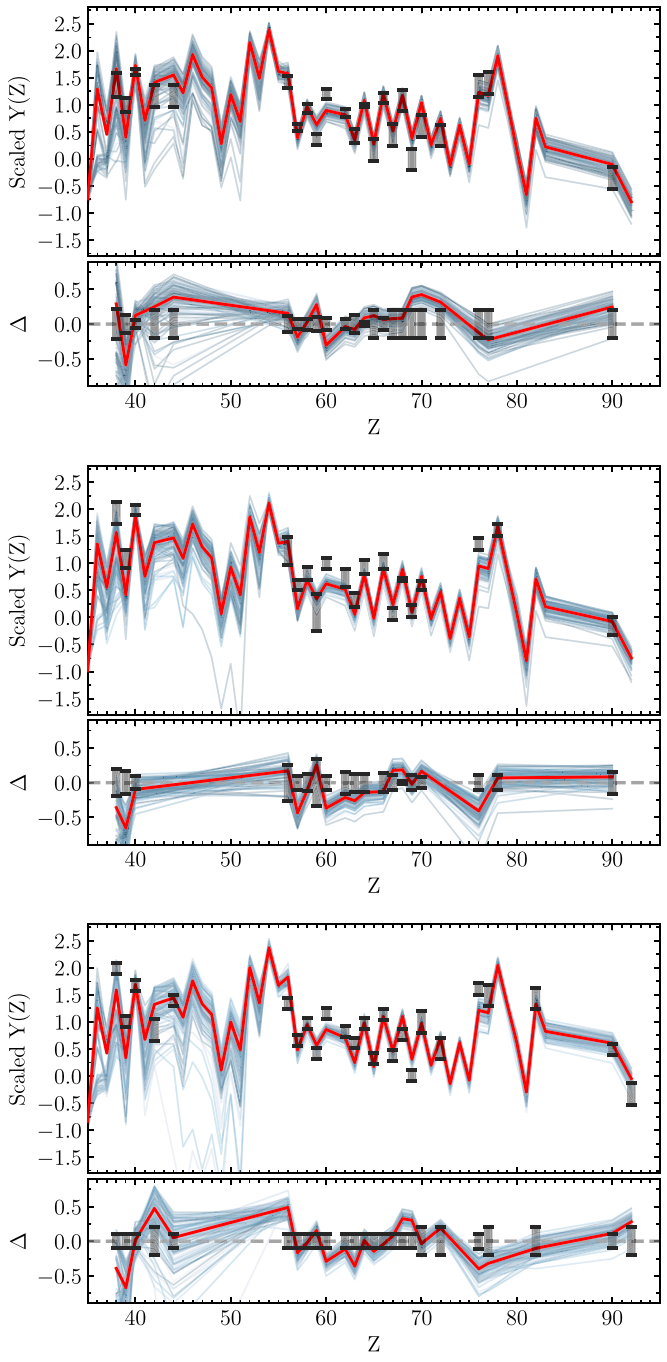

Figure 5. Final combined abundance pattern results (red lines) of the ADM model when matching Ret II (top), Group F (middle), and J0954+5246 (bottom) abundances. Successes of individual runs are shown in blue.

$Y_e \approx 0.18$ coincides with maximal actinide production and (locally) minimal lanthanide production when using this trajectory (see Figure 3), producing a $\log \epsilon(\mathrm{Th/Dy})$ ratio that is much higher than what observations suggest.

Figure 5 shows the final abundance patterns for the ejecta distributions shown in Figure 4. Every individual abundance pattern (blue) represents a successful set of the N random Y_e choices made in the ADM method. Each combined abundance pattern (red) succeeds in reproducing the scaled abundances of the limited-r elements and many of the lanthanide elements. The common dip surrounding $Z = 60$ (Nd) is mostly due to the strong shell closures of FRDM2012, and partially due to the

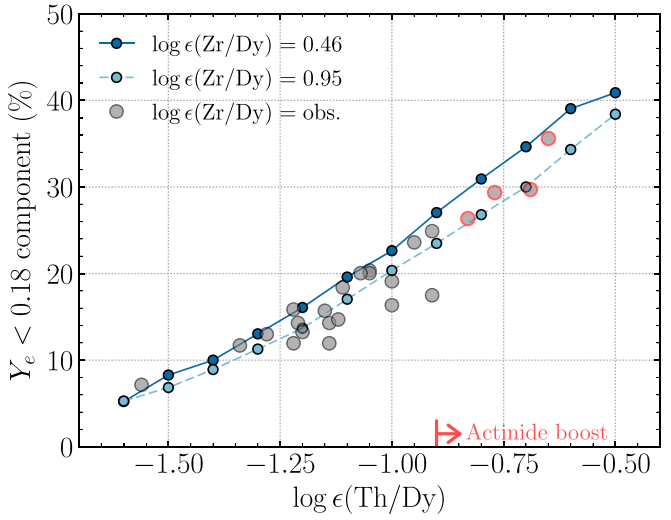

Figure 6. Percentage of allowed very low Y_e (<0.18), actinide-rich mass to reproduce various $\log \epsilon(\mathrm{Th/Dy})$ abundances, while requiring the specified $\log \epsilon(\mathrm{Zr/Dy})$ ratio. Gray dots show the ADM model applied to select r-process stars with observed $\log \epsilon(\mathrm{Zr/Dy})$ and $\log \epsilon(\mathrm{Th/Dy})$ ratios as input constraints (Placco et al. 2017; Abohalima & Frebel 2018; Holmbeck et al. 2018; Sakari et al. 2018).

pure symmetric fission fragment yields we employ. However, this underproduction does not have any influence over the results we present here. We finally note that for all three stellar groups, we have only supplied three abundance constraints to the ADM model. Hence, with few constraints, relatively good agreements across the entire r-process patterns are produced.

4.1. The Low-Y_e Component

The largest difference in the empirical Y_e distributions of ejecta with varying levels of actinide enhancement lies in the allowed mass produced in very low-Y_e environments. To investigate this difference in detail, we systematically vary the ADM model input $\log \epsilon(\mathrm{Th/Dy})$ constraint while holding the $\log \epsilon(\mathrm{Zr/Dy})$ constraint constant. This way, we can quantify the amount of very low-Y_e material that the progenitor r-process event may eject. We repeat this process twice, once holding the $\log \epsilon(\mathrm{Zr/Dy})$ constraint at 0.46 and again at 0.95, following the labeled bounds in Figure 1 (top panel). Recall that these bounds contain r-process-enhanced stars in which the r-process material likely originated from one r-process event. These systematic results are also compared to ADM results using both the $\log \epsilon(\mathrm{Th/Dy})$ and $\log \epsilon(\mathrm{Zr/Dy})$ observational abundance ratios from single r-process-enhanced stars in the bottom panel of Figure 1.

Systematically varying the $\log \epsilon(\mathrm{Th/Dy})$ input constraint shows a smoothly increasing fraction of allowed ejecta masses at very low-Y_e. The r-process-enhanced stars with likely single r-process progenitors fall between the two calculated curves (blue solid and dashed lines) in Figure 6, by definition. Most of these stars thus allow about 10% to 25% of their progenitor's r-process ejecta mass to be at $Y_e < 0.18$. The actinide-boost stars found at $\log \epsilon(\mathrm{Th/Dy}) > -0.90$ allow roughly 25% to 35% of this very low-Y_e material. This enhancement accounts for increased actinide abundances. Stars falling below the lower curve are those with higher $\log \epsilon(\mathrm{Zr/Dy})$ ratios, which formed from gas that was likely polluted by multiple events. Assuming the r-process signature in stars with higher $\log \epsilon(\mathrm{Zr/Dy})$ originated from a single event, the ADM model can then

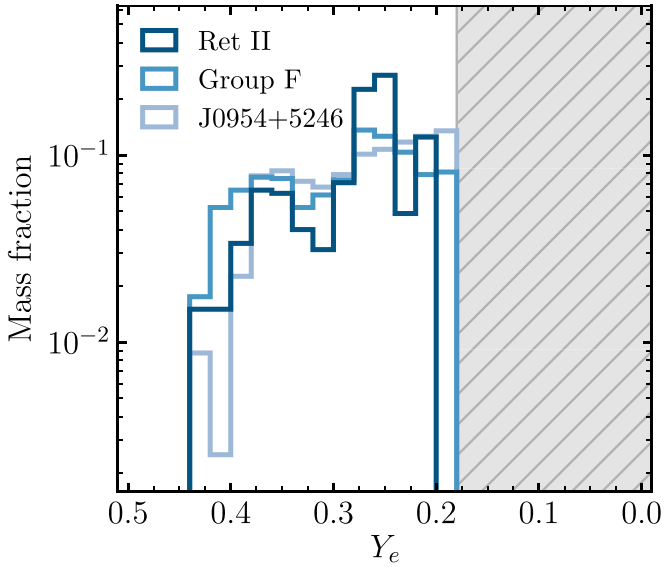

Figure 7. Ejecta distribution results for all three cases allowing no $Y_e < 0.18$.

account for their observed *r*-process element distributions using a mass ejecta distribution that is shifted to higher-Y_e values.

Our ADM model results do not indicate a clear separation between the actinide-boost stars and their non-actinide-enhanced counterparts. This agrees with the observed actinide abundances which suggests a smooth distribution of actinide enhancements, with the actinide-boost stars populating a low-probability tail of this distribution. This indicates that the same *r*-process source can produce all levels of actinide enrichment seen in *r*-process-enhanced stars. Different levels of actinide enhancement would then reflect a slightly different distribution in the mass ejecta properties within the *r*-process progenitor. In all cases, the amount of fission-cycled (in this trajectory, $Y_e < 0.18$) material required to reproduce our *r*-process abundance observations may be a significant—but not dominant—fraction of the entire *r*-process mass ejecta as it sensitively affects the actinide contribution.

Interestingly, the abundance ratios can still be reproduced by the ADM model when the very low-Y_e component is omitted entirely. We investigate this effect by repeating the ADM calculation, only allowing the model to sample at $0.18 \leqslant Y_e \leqslant 0.45$. These results are shown in Figure 7. Disallowing Y_e below 0.18 produces a somewhat bimodal distribution driven by the $\log \epsilon(\mathrm{Zr/Dy})$ and $\log \epsilon(\mathrm{Th/Dy})$ requirements. For Ret II and Group F, a peak forms at $Y_e \approx 0.25$, coinciding with the single Y_e that satisfies the input $\log \epsilon(\mathrm{Th/Dy})$ ratio. Since now no Th can come from $Y_e < 0.18$, all the Th contribution is concentrated around this Y_e. However, for the actinide-boost case, not enough Th is produced at $Y_e \approx 0.25$, and the ejecta mass builds up near the cutoff at $Y_e = 0.18$, where actinides are still able to be synthesized at levels necessary to eventually reproduce observed stellar abundances, within the allowed ranges of Table 1. With the total amount of Dy constrained mostly by contributions from the $Y_e = 0.25$ region, the Zr abundance primarily comes from higher values of Y_e. This restraint produces the broad peak around $Y_e = 0.37$. Although these precise Y_e constraints are mildly dependent on other astrophysical parameters (discussed in Section 5), we conclude that it is possible to reproduce the abundance patterns seen in *r*-process-enhanced stars without fission cycling (for the conditions considered here, meaning without $Y_e \lesssim 0.25$ material), but such a

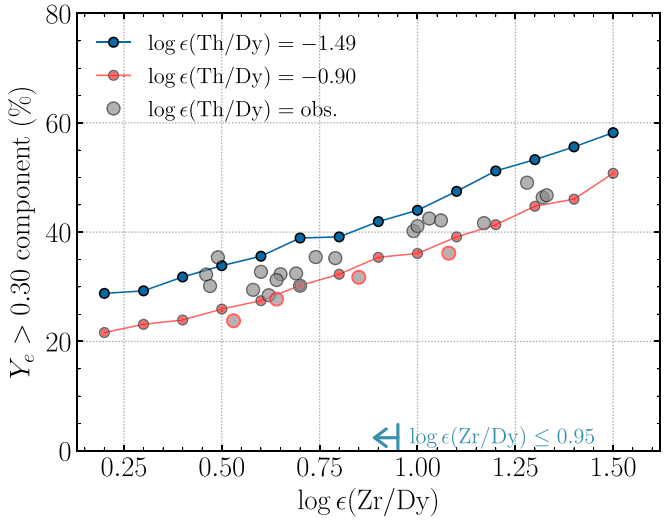

Figure 8. Percentage of allowed $Y_e > 0.3$, Zr-rich mass to reproduce various $\log \epsilon(\mathrm{Zr/Dy})$ abundances with constant $\log \epsilon(\mathrm{Th/Dy})$ ratio constraints. Gray dots show the ADM model applied to select *r*-process stars with their observed $\log \epsilon(\mathrm{Zr/Dy})$ and $\log \epsilon(\mathrm{Th/Dy})$ ratios as input constraints (Placco et al. 2017; Abohalima & Frebel 2018; Holmbeck et al. 2018; Sakari et al. 2018), with red circles denoting the actinide-boost stars.

cutoff places stricter and more finely tuned requirements on the distribution of Y_e in the ejecta.

The ADM model would fail for Ret II if a Y_e cutoff of 0.23 or greater was applied because there is simply not enough actinide material produced. Similarly, applying a cutoff at $Y_e \geqslant 0.21$ would prevent the ADM model from reproducing actinide-boost abundance ratios. As seen in Figure 3, the Th abundance rises rapidly as Y_e decreases from 0.24 to 0.17, covering over four dex—and thus all observed levels—of actinide abundance. It is therefore unsurprising that the ADM model consistently favors this range. Next, we turn to the higher-Y_e component which contributes the bulk of the ejected Zr (i.e., limited-*r*) material.

4.2. The Higher-Y_e Component

In analogy to Figure 6 of the very low-Y_e component fraction, Figure 8 shows the allowed fraction of material ejected at $Y_e > 0.30$ as a function of the input $\log \epsilon(\mathrm{Zr/Dy})$ constraint to characterize the limited-*r* contribution from single *r*-process events. The ADM model is run multiple times varying the input $\log \epsilon(\mathrm{Zr/Dy})$ while holding the $\log \epsilon(\mathrm{Th/Dy})$ constant, first at the actinide-boost cutoff (−0.90) and then at the very actinide-poor value following Ret II (−1.49). The ejecta mass fraction with $Y_e > 0.30$ is also shown for individual stars using their observational $\log \epsilon(\mathrm{Zr/Dy})$ and $\log \epsilon(\mathrm{Th/Dy})$ abundance ratios as constraints.

Figure 8 suggests that in order for the *r*-process event to synthesize all the required limited-*r* material as well as the main *r*-process material, a minimum of roughly 25% of the mass must be ejected at $0.30 < Y_e \leqslant 0.45$. For stars with $\log \epsilon(\mathrm{Zr/Dy}) \leqslant 0.95$—which likely received their *r*-process material from only one progenitor—between roughly 25% and 35% of the progenitor ejecta mass has $0.30 < Y_e \leqslant 0.45$. Furthermore, because there is an observational minimum of $\log \epsilon(\mathrm{Zr/Dy}) \approx 0.46$, our ADM model results imply that at least ∼25% of the *r*-process ejecta mass must be ejected at these higher values of Y_e.

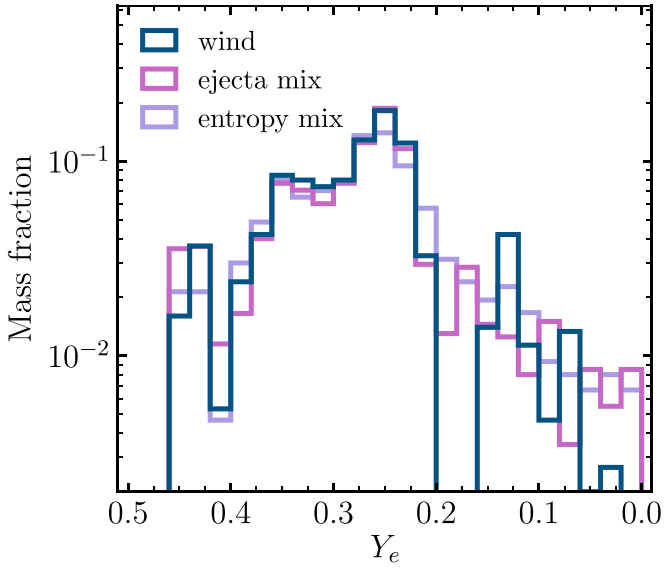

Figure 9. Ejecta distribution predicted by the ADM model matching Ret II abundances using the disk wind trajectory only ("wind"), an NSM represented by a combination of wind and tidal ejecta ("ejecta mix"), and a combination of different entropies ("entropy mix"). All simulations use the FRDM2012 mass model.

If the material in stars with $\log \epsilon(\mathrm{Zr/Dy}) > 0.95$ were to originate from a single *r*-process progenitor, then more than 40% of the *r*-process ejecta must be at $Y_e > 0.30$. However, as previously noted, the main *r*-process material found in stars moderately enhanced in *r*-process elements with $\log \epsilon(\mathrm{Zr/Dy}) > 0.95$ could have been diluted by limited-*r*-only events such as CCSN neutrino-driven winds that primarily produce the limited-*r*-process elements (Arcones & Thielemann 2013; Wanajo 2013).

5. Model Variations

In this section, we investigate the impact that both astrophysical and nuclear physics variations have on the results of our ADM model to test the robustness of these empirically built mass ejecta distributions.

5.1. Astrophysical Sites

The previous calculations only consider the *r*-process originating from a single site, an accretion disk wind. Two situations that might occur in "realistic" astrophysical *r*-process events are a mix of ejecta types and a mix of different entropies. One promising *r*-process production site is the very low-Y_e tidal ejecta of an NSM. We choose a low-entropy ($s/k \approx 10$) trajectory from the 1.4–1.4 $M_\odot$ NSM simulations by S. Rosswog as in Korobkin et al. (2012) for the tidal ejecta. Next, we vary the initial Y_e between 0.005 and 0.180 and run full *r*-process calculations for this tidal ejecta trajectory. Then we used the ADM model to randomly sample from only the tidal ejecta component at $Y_e < 0.13$, and from only the wind component at $Y_e \geqslant 0.18$. For the region at $0.13 \leqslant Y_e < 0.18$, the ADM model samples from both the tidal and wind ejecta with equal probability, producing a mixed-ejecta distribution. This combination may be one representation of total NSM ejecta undergoing an *r*-process. Figure 9 shows the empirical Y_e distribution obtained by using a combination of wind and tidal ejecta which match the Ret II abundances ("ejecta mix"). Although the $Y_e < 0.18$ component is distributed differently in the mixed ejecta case than the wind-only counterpart, the amount of necessary $Y_e < 0.18$ mass from the tidal ejecta is similar to that of the wind.

The *r*-process can also feasibly occur in an environment that supports a range of entropies. We investigate the effect of entropy on the Y_e distribution by repeating the simulations with a high entropy ($s/k \approx 85$) trajectory for the entire range of $0.005 \leqslant Y_e \leqslant 0.450$ in equal steps, and extended the very low entropy tidal trajectory to $Y_e \leqslant 0.250$. Next, the ADM model was run, randomly sampling between the original disk wind trajectory and the high entropy trajectory for $0.250 < Y_e \leqslant 0.450$, and between the low, medium, and high entropy trajectories for $0.005 \leqslant Y_e \leqslant 0.250$. The ejecta distribution results from the ADM model using a random combination of entropies are shown in Figure 9 ("entropy mix").

The previously mentioned dip at $Y_e \approx 0.18$ disappears when combining trajectories with different astrophysical properties. This is because the value $Y_e = 0.18$ does not universally signify robust actinide production for all *r*-process trajectories. In the lowest entropy (tidal ejecta) trajectory, the Th abundance peaks at the lower Y_e of 0.125. At $Y_e = 0.18$, instead of a peak in Th production occurring—as that produced by the high and medium entropy (wind) trajectories—the very low-entropy tidal ejecta trajectory produces a Dy peak, allowing the mass at $Y_e \approx 0.18$ to satisfy the input abundance ratio constraints and wash out the apparent two-component Y_e distribution.

In summary, considering variations in the astrophysical site slightly affects the details of the predicted ejecta mass distribution. However, qualitatively, the ADM model robustly suggests that if there is any low-Y_e fission-cycling ejecta component, it must be small compared to the *r*-process material ejected by the disk wind at higher-Y_e.

5.2. Nuclear Physics Inputs

Nucleosynthesis calculations of the *r*-process rely heavily on theoretical data to attempt estimates of reaction rates for very unstable (and as of yet unmeasured) nuclei along the *r*-process path. Using different prescriptions of nuclear data far from stability can lead to dramatic differences in both the extent of the *r*-process and the final shape of the abundance pattern (e.g., Kratz et al. 1993, 1998; Wanajo et al. 2004; Mumpower et al. 2016). We test the robustness of the ADM model results by repeating our calculations using nuclear data informed by the Duflo–Zuker (DZ; Duflo & Zuker 1995) and the Hartree–Fock-Bogoliubov (HFB; Goriely et al. 2009) mass models. We use theoretical reaction and decay rates recalculated to be consistent with each mass model and use HFB barrier heights for fission rates within this mass model as in Vassh et al. (2019). Figure 10 shows the results using the disk wind trajectory and three different nuclear mass models, using the Ret II abundance constraints. Although using DZ and HFB mass models results in ADM distributions with more low-Y_e mass, the relative shape and magnitude of higher-Y_e material reflects our results found when using the FRDM2012 mass model.

5.3. The Low-Y_e Component

As seen in Figure 10, the amount of predicted very low-Y_e ejecta mass varies with mass model. In contrast, Figure 9 displays little variation when using a mix of ejecta types or

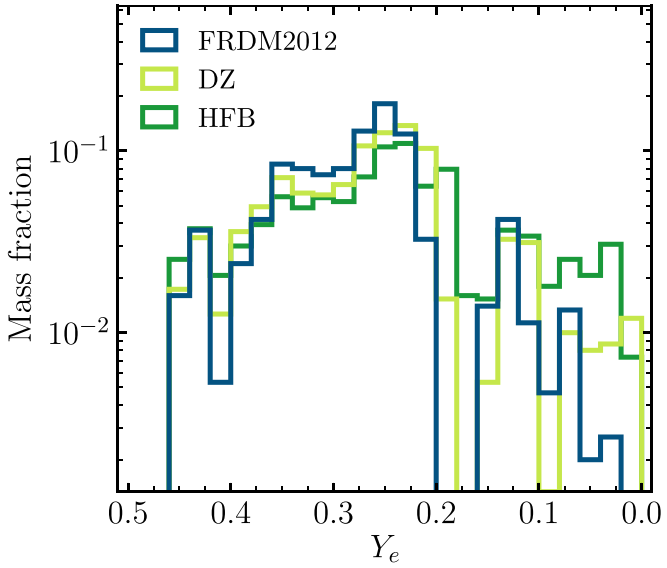

Figure 10. ADM predictions for Ret II using a disk wind trajectory and the FRDM2012 (blue), DZ (light green), and HFB (dark green) mass models.

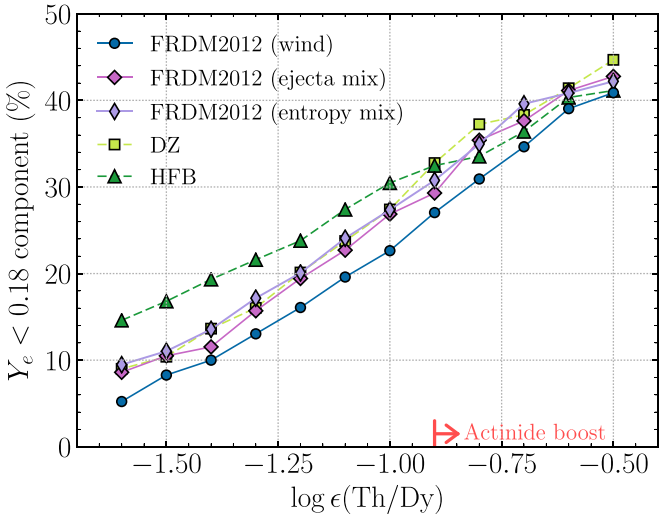

Figure 11. Percentage of allowed very low Y_e (<0.18), actinide-rich mass to reproduce various log ϵ(Th/Dy) abundances constraining the log ϵ(Zr/Dy) to be the Ret II value for each mass model specified.

entropies. In Figure 11, we quantify the fraction of very low-Y_e mass that the ADM model predicts is ejected when applying nuclear and astrophysical variations across a range of actinide abundances. The DZ mass model tends to allow ∼5% more very low-Y_e material than FRDM2012 as simulations using the DZ mass model do not produce the actinides as robustly as with FRDM2012 (Holmbeck et al. 2019). Similarly, material leaves the actinide region due to higher neutron-induced reaction flows at later times with the HFB mass model compared to when using FRDM2012, also producing a lower final actinide abundance. As a result, using HFB masses allows for ⩽10% more low-Y_e mass than when employing FRDM2012. Using a combination of tidal and wind ejecta or a combination of entropies slightly boosts the allowed very low-Y_e mass; however, the astrophysical variations lie comfortably within uncertainties in the nuclear masses.

In summary, accounting for nuclear mass model variations, the very low-Y_e ejected mass fractions may be as high as 40% to account for most observations of actinides in *r*-process-enhanced metal-poor stars. Our results are robust under changes to the nuclear physics, with a variation of the allowed low-Y_e component of ∼10% of the total mass when considering variations to nuclear mass models or astrophysical environments.

6. The GW170817 Associated Kilonova

A parameterized accretion disk trajectory—and the conclusions drawn from using this trajectory—is consistent with one possible description of NSM ejecta environments. However, these conclusions are not necessarily unique and could still be applicable to other astrophysical sites, such as collapsars. Here we test if the ADM model results agree with what has been inferred from the GW170817 associated kilonova ("SSS17a" or "AT 2017gfo"). This could offer another hint for NSMs as primary *r*-process sources of material in early, small emerging dwarf galaxies that gave rise to the *r*-process-enhanced stars.

Cowperthwaite et al. (2017) proposed that the light curve AT 2017gfo could only be explained by multiple components: a lanthanide-poor ("blue") and lanthanide-rich ("red") component. Inspired by this two-component model, we split our ADM model Y_e distributions for Ret II into a blue and a red component. We define the blue component as primarily producing limited-*r* elements, extending over a range of $0.29 < Y_e \leqslant 0.45$ (recall Figure 3), and the red component consisting of the remaining material at $Y_e \geqslant 0.29$. Using these ranges, we find lanthanide mass fractions of $X_{\rm lan} = 10^{-0.8}$ for the red and $X_{\rm lan} = 10^{-3.8}$ for the blue components when using our ADM model. The mass ratio between these components is $m_{\rm red}/m_{\rm blue} = 1.7$.

Kasen et al. (2017) also invoke a two-component model to resemble AT 2017gfo, based on the high opacity of lanthanide elements that would produce an extended emission spectrum. For their models to agree with AT 2017gfo, a lanthanide-rich red kilonova would need to have a lanthanide mass fraction of $X_{\rm lan} \sim 10^{-1.5}$, and the lanthanide-poor blue kilonova would need to have $X_{\rm lan} \sim 10^{-4}$. The ejecta mass ratio they estimate between these components is $m_{\rm red}/m_{\rm blue} = 1.6$.

The lanthanide mass fractions extracted from our model are slightly larger than those found by Kasen et al. (2017). Our ADM simulations do not extend to iron-peak elements, which could be produced in higher-Y_e regions during an NSM event. Adding a contribution from iron-peak ejecta could bring our lanthanide mass fractions into further agreement with results by Kasen et al. (2017). Overall, our results agree, despite our inherently different approaches.

7. Conclusions

Using elemental abundances of *r*-process-enhanced metal-poor stars, we have constructed empirical Y_e distributions describing the ejecta of *r*-process events through the ADM model. We find that the *r*-process abundance signatures of actinide-boost and actinide-deficient stars can likely originate from variations in Y_e distribution of ejecta from the same type of astrophysical *r*-process event. Both observationally and in the ADM model results, there is no clear point or distinct set of conditions at which the actinide-boost activates. Rather, the smoothness of the distribution of observed actinide abundances

correlates well with the smooth growth of the allowed very low-Y_e tail of our ADM ejecta mass distributions, as seen in Figures 6 and 11.

Most actinide enrichments of metal-poor, *r*-process-enhanced stars can be explained by an *r*-process source with a very neutron-rich, fission-cycling component. We estimate this fission-cycling ejecta to be a nondominant (10%–30%) constituent of the *r*-process ejecta mass. All levels of limited-*r* abundance with respect to the lanthanides in stars with $\log \epsilon(\mathrm{Zr/Dy}) \leqslant 0.95$ can be straightforwardly accommodated within the same *r*-process source. For these stars, the lanthanide-poor component, which is rich in limited-*r* elements, constitutes about 25%–40% of the ejecta mass. This suggests that the *r*-process material in these stars need only come from one site that can produce the entire observed relative *r*-process abundance range from Sr to U.

The *r*-process signatures of very metal-poor stars allow the study of single *r*-process events, which we have characterized through the ADM model. We compared our empirically found progenitor Y_e distributions of ejecta to the results of an independent study of the currently favored *r*-process site, an NSM. We found that both the lanthanide mass fraction and the red-to-blue mass ejecta ratio derived from the ADM model are consistent with results matching the light curve of the GW170817 associated kilonova, AT 2017gfo. The shape of our empirical Y_e distributions also resemble those extracted from available hydrodynamical NSM simulations (Fernández et al. 2015; Radice et al. 2018). However, the accretion disk wind used in this work may be theoretically similar to—or perhaps even observationally indistinguishable from—other astrophysical sites, e.g., the accretion disk wind from a collapsar remnant. Explicitly calculating the lanthanide mass fraction from stellar abundances, Ji et al. (2019) also find larger lanthanide mass fractions than studies of the AT2017gfo kilonova. These authors argue that if NSMs are the dominant source of *r*-process material, future kilonovae observations should find much higher lanthanide mass fractions than for GW170817. If future follow-up of LIGO/aLIGO detections do not find high lanthanide mass fractions of material ejected by NSM events, then another site must be invoked to account for *r*-process production in the early universe. Upcoming LIGO/aLIGO detections of NSMs and follow-up observations of their electromagnetic counterparts will be helpful to further characterize the progenitor site(s) of *r*-process-enhanced stars and determine whether NSMs are the dominant source of *r*-process material in the early universe.

In addition to investigations of NSMs and other *r*-process events, a comprehensive study of the *r*-process calls for more observations of metal-poor stars enhanced in these elements. Further identifications of *r*-II stars and their elemental abundances can be used to progress several areas of *r*-process studies. For example, more measurements of Th can test if DES J033523−540407 in Ret II and J0954+5246 in the halo represent limits on Th/Dy production, or if an even broader range exists. Large actinide variations at higher metallicities could indicate activity by other *r*-process sources as a function of chemical evolution, which can be identified and characterized through theoretical tools such as the ADM. Although Th abundances have not been determined in all *r*-process-enhanced stars, many upper limits on stellar Th abundances are available. Results derived through an adapted ADM model from those upper limits on Th could set meaningful constraints on, e.g., the maximum allowed very low-Y_e material for *r*-process events if all *r*-process-enhanced stars share a progenitor site. Detailed spectroscopy of more *r*-II stars will also allow further measurements of U. Due to the observed spread in abundance ratios, there is currently no unifying set of actinide-to-lanthanide production ratios that can be unilaterally applied to carry out cosmochronometry. However, the U/Th ratio principally remains a robust and reliable tool for radioactive decay dating if ejecta distributions built from observed elemental patterns could be used to refine the required type of production ratios that accurately reflect the relevant progenitor site(s).

Overall, larger numbers of known *r*-II stars would increase and/or refine identifications of kinematic groups in the Galactic halo as well as enable additional Th and U measurements. Hence, a main objective of the *R*-Process Alliance (RPA; Hansen et al. 2018; Sakari et al. 2018; Aprahamian et al. 2018) is to increase the number of known *r*-II stars from ∼30 to ∼100. Applying information from additional statistically significant kinematic groupings to the ADM model could then be used to investigate whether NSMs are main sources of *r*-process material, or if the ADM suggests that other *r*-process sources are predominantly needed.

The wealth of stellar abundance data—from surveys such as that being conducted by the RPA—together with theoretical *r*-process studies, future NSM detections, and nuclear physics constraints from next-generation rare-isotope beam facilities (e.g., FRIB) will allow thorough investigations of the origins of all *r*-process elements.

This work was initiated by discussions at the FRIB Theory Alliance workshop, "FRIB and the GW170817 kilonova" (Aprahamian et al. 2018), which was supported by the U.S. Department of Energy (DOE) through the FRIB Theory Alliance under Contract No. DE-SC0013617. The authors also benefited from support by the National Science Foundation (NSF) under grant No. PHY-1430152 (JINA Center for the Evolution of the Elements). A.F. is partially supported by National Science Foundation grant AST-1716251. This work was supported in part by the U.S. DOE under contract Nos. DE-FG02-02ER41216 (G.C.M.), DE-FG02-95-ER40934 and DE-SC0018232 (R.S. and T.M.S.), and DE-AC52-07NA27344 for the topical collaboration Fission In R-process Elements (FIRE; G.C.M., R.S., and M.R.M.), and by the NSF under contract No. PHY-1630782 (N3AS; G.C.M. and R.S.). M.R.M. was supported by the US DOE through the Los Alamos National Laboratory operated by Triad National Security, LLC, for the National Nuclear Security Administration of U.S. DOE (Contract No. 89233218CNA000001).

Software: Numpy (van der Walt et al. 2011), Matplotlib (Hunter 2007).

ORCID iDs

Erika M. Holmbeck https://orcid.org/0000-0002-5463-6800
Anna Frebel https://orcid.org/0000-0002-2139-7145
G. C. McLaughlin https://orcid.org/0000-0001-6811-6657
Matthew R. Mumpower https://orcid.org/0000-0002-9950-9688
Trevor M. Sprouse https://orcid.org/0000-0002-4375-4369
Rebecca Surman https://orcid.org/0000-0002-4729-8823

References

Abbott, B. P., Abbott, R., Abbott, T. D., et al. 2017, PhRvL, 119, 161101
Abohalima, A., & Frebel, A. 2018, ApJS, 238, 36
Andrievsky, S. M., Spite, F., Korotin, S. A., et al. 2011, A&A, 530, A105
Aprahamian, A., Surman, R., Frebel, A., et al. 2018, arXiv:1809.00703
Arcones, A., & Thielemann, F.-K. 2013, JPhG, 40, 013201
Barklem, P. S., Christlieb, N., Beers, T. C., et al. 2005, A&A, 439, 129
Beers, T. C., & Christlieb, N. 2005, ARA&A, 43, 531
Bramante, J., & Linden, T. 2016, ApJ, 826, 57
Brauer, K., Ji, A. P., Frebel, A., et al. 2019, ApJ, 871, 247
Burbidge, E. M., Burbidge, G. R., Fowler, W. A., & Hoyle, F. 1957, RvMP, 29, 547
Cameron, A. G. W. 2003, ApJ, 587, 327
Côté, B., Eichler, M., Arcones, A., et al. 2019, ApJ, 875, 106
Côté, B., Fryer, C. L., Belczynski, K., et al. 2018, ApJ, 855, 99
Cowan, J. J., Pfeiffer, B., Kratz, K.-L., et al. 1999, ApJ, 521, 194
Cowperthwaite, P. S., Berger, E., Villar, V. A., et al. 2017, ApJL, 848, L17
Drout, M. R., Piro, A. L., Shappee, B. J., et al. 2017, Sci, 358, 1570
Duflo, J., & Zuker, A. P. 1995, PhRvC, 52, R23
Eichler, M., Arcones, A., Kelic, A., et al. 2015, ApJ, 808, 30
Farouqi, K., Kratz, K.-L., Pfeiffer, B., et al. 2010, ApJ, 712, 1359
Fernández, R., Kasen, D., Metzger, B. D., & Quataert, E. 2015, MNRAS, 446, 750
Frebel, A. 2018, ARNPS, 68, 237
Freiburghaus, C., Rosswog, S., & Thielemann, F.-K. 1999, ApJL, 525, L121
Fuller, G. M., Kusenko, A., & Takhistov, V. 2017, PhRvL, 119, 061101
Goriely, S., Chamel, N., & Pearson, J. M. 2009, PhRvL, 102, 152503
Hansen, C. J., Primas, F., Hartman, H., et al. 2012, A&A, 545, A31
Hansen, T. T., Holmbeck, E. M., Beers, T. C., et al. 2018, ApJ, 858, 92
Hansen, T. T., Simon, J. D., Marshall, J. L., et al. 2017, ApJ, 838, 44
Holmbeck, E. M., Beers, T. C., Roederer, I. U., et al. 2018, ApJL, 859, L24
Holmbeck, E. M., Sprouse, T. M., Mumpower, M. R., et al. 2019, ApJ, 870, 23
Hunter, J. D. 2007, CSE, 9, 90
Ji, A. P., Drout, M. R., & Hansen, T. T. 2019, arXiv:1905.01814
Ji, A. P., & Frebel, A. 2018, ApJ, 856, 138
Ji, A. P., Frebel, A., Chiti, A., & Simon, J. D. 2016a, Natur, 531, 610
Ji, A. P., Frebel, A., Simon, J. D., & Chiti, A. 2016b, ApJ, 830, 93
Kasen, D., Metzger, B., Barnes, J., Quataert, E., & Ramirez-Ruiz, E. 2017, Natur, 551, 80
Kawano, T., Capote, R., Hilaire, S., & Chau Huu-Tai, P. 2016, PhRvC, 94, 014612
Kilpatrick, C. D., Foley, R. J., Kasen, D., et al. 2017, Sci, 358, 1583
Kodama, T., & Takahashi, K. 1975, NuPhA, 239, 489
Korobkin, O., Rosswog, S., Arcones, A., & Winteler, C. 2012, MNRAS, 426, 1940
Kratz, K.-L., Bitouzet, J.-P., Thielemann, F.-K., Moeller, P., & Pfeiffer, B. 1993, ApJ, 403, 216
Kratz, K.-L., Pfeiffer, B., & Thielemann, F.-K. 1998, NuPhA, 630, 352
Lattimer, J. M., & Schramm, D. N. 1974, ApJL, 192, L145
Malkus, A., McLaughlin, G. C., & Surman, R. 2016, PhRvD, 93, 045021
Mashonkina, L., Christlieb, N., & Eriksson, K. 2014, A&A, 569, A43
Metzger, B. D., Piro, A. L., & Quataert, E. 2008, MNRAS, 390, 781
Meyer, B. S. 1989, ApJ, 343, 254
Möller, P., Mumpower, M. R., Kawano, T., & Myers, W. D. 2019, ADNDT, 125, 1
Möller, P., Myers, W. D., Sagawa, H., & Yoshida, S. 2012, PhRvL, 108, 052501
Möller, P., Sierk, A. J., Ichikawa, T., Iwamoto, A., & Mumpower, M. 2015, PhRvC, 91, 024310
Möller, P., Sierk, A. J., Ichikawa, T., & Sagawa, H. 2016, ADNDT, 109, 1
Mösta, P., Roberts, L. F., Halevi, G., et al. 2018, ApJ, 864, 171
Mumpower, M. R., Kawano, T., Sprouse, T. M., et al. 2018, ApJ, 869, 14
Mumpower, M. R., Kawano, T., Ullmann, J. L., Krtička, M., & Sprouse, T. M. 2017, PhRvC, 96, 024612
Mumpower, M. R., Surman, R., McLaughlin, G. C., & Aprahamian, A. 2016, PrPNP, 86, 86
Nishimura, N., Takiwaki, T., & Thielemann, F.-K. 2015, ApJ, 810, 109
Perego, A., Rosswog, S., Cabezón, R. M., et al. 2014, MNRAS, 443, 3134
Placco, V. M., Holmbeck, E. M., Frebel, A., et al. 2017, ApJ, 844, 18
Pruet, J., Thompson, T. A., & Hoffman, R. D. 2004, ApJ, 606, 1006
Radice, D., Perego, A., Hotokezaka, K., et al. 2018, ApJ, 869, 130
Ren, J., Christlieb, N., & Zhao, G. 2012, A&A, 537, A118
Roederer, I. U. 2013, AJ, 145, 26
Roederer, I. U., Hattori, K., & Valluri, M. 2018, AJ, 156, 179
Roederer, I. U., Jacobson, H. R., Thanathibodee, T., Frebel, A., & Toller, E. 2014a, ApJ, 797, 69
Roederer, I. U., Mateo, M., Bailey, J. I., III, et al. 2016, AJ, 151, 82
Roederer, I. U., Preston, G. W., Thompson, I. B., et al. 2014b, AJ, 147, 136
Safarzadeh, M., Ramirez-Ruiz, E., Andrews, J. J., et al. 2019, ApJ, 872, 105
Sakari, C. M., Placco, V. M., Hansen, T., et al. 2018, ApJL, 854, L20
Schatz, H., Toenjes, R., Pfeiffer, B., et al. 2002, ApJ, 579, 626
Schlaufman, K. C., Rockosi, C. M., Allende Prieto, C., et al. 2009, ApJ, 703, 2177
Searle, L., & Zinn, R. 1978, ApJ, 225, 357
Shappee, B. J., Simon, J. D., Drout, M. R., et al. 2017, Sci, 358, 1574
Siegel, D. M., Barnes, J., & Metzger, B. D. 2019, Natur, 569, 241
Siqueira Mello, C., Hill, V., Barbuy, B., et al. 2014, A&A, 565, A93
Surman, R., Beun, J., McLaughlin, G. C., Kane, S., & Hix, W. R. 2008, JPhG, 35, 014059
Surman, R., & McLaughlin, G. C. 2004, ApJ, 603, 611
Thielemann, F.-K., Arcones, A., Käppeli, R., et al. 2011, PrPNP, 66, 346
Travaglio, C., Gallino, R., Arnone, E., et al. 2004, ApJ, 601, 864
Tumlinson, J. 2010, ApJ, 708, 1398
van der Walt, S., Colbert, S. C., & Varoquaux, G. 2011, CSE, 13, 22
Vassh, N., Vogt, R., Surman, R., et al. 2019, JPhG, 46, 065202
Wanajo, S. 2013, ApJL, 770, L22
Wanajo, S., Goriely, S., Samyn, M., & Itoh, N. 2004, ApJ, 606, 1057
Wanajo, S., Itoh, N., Ishimaru, Y., Nozawa, S., & Beers, T. C. 2002, ApJ, 577, 853
Westin, J., Sneden, C., Gustafsson, B., & Cowan, J. J. 2000, ApJ, 530, 783
Winteler, C., Käppeli, R., Perego, A., et al. 2012, ApJL, 750, L22
Zagrebaev, V. I., Karpov, A. V., Mishustin, I. N., & Greiner, W. 2011, PhRvC, 84, 044617
Zhu, Y., Wollaeger, R. T., Vassh, N., et al. 2018, ApJL, 863, L23